

Type-II Dirac states in full Heusler compounds XInPd_2 ($\text{X} = \text{Ti, Zr and Hf}$)

Chiranjit Mondal,^{1,*} Chanchal K. Barman,^{2,*} Biswarup Pathak,^{1,3,†} and Aftab Alam^{2,‡}

¹*Discipline of Metallurgy Engineering and Materials Science, IIT Indore, Simrol, Indore 453552, India*

²*Department of Physics, Indian Institute of Technology, Bombay, Powai, Mumbai 400076, India*

³*Discipline of Chemistry, School of Basic Sciences, IIT Indore, Simrol, Indore 453552, India*

(Dated: March 13, 2024)

We predict three full Heusler compounds XInPd_2 ($\text{X} = \text{Zr, Hf and Ti}$) to be potential candidates for type-II Dirac semimetals. The crystal symmetry of these compounds have appropriate chemical environment with a unique interplay of inversion, time reversal and mirror symmetry. These symmetries help to give six pairs of type-II Dirac nodes on the C_4 rotation axis, closely located at/near the Fermi level. Using first principle calculations, symmetry arguments and crystal field splitting analysis, we illustrate the occurrence of such Dirac nodes in these compounds. Bulk Fermi surfaces have been studied to understand the Lorentz symmetry breaking and Lifshitz transition (LT) of Fermi surfaces. Bulk nodes are projected on the (001) and (111) surfaces which form the surface Fermi arcs, that can further be detected by probes such as angle resolved photo-emission and scanning tunneling spectroscopy. By analyzing the evolution of arcs with changing chemical potential, we prove the fragile nature and the absence of topological protection of the Dirac arcs. Our predicted compounds overcome the limitations of the previously reported PtTe_2 class of compounds.

Introduction: Collective excitation of elementary electrons warrants several distinct Fermionic behavior in condense matter systems. These Fermions can be classified as Dirac, Majorana, Weyl, triple-point, nodal-line semimetal etc. Although the Dirac Fermions have been realized in high energy experiments, the Weyl and Majorana had not so far been observed until the discovery of topological semimetals and superconductors in low energy condense matter systems. Dirac semimetals (DSM)^{1,2} and Weyl semimetals (WSM)^{3,4} are the well known topological materials with surface states (SSs) driven Fermi arcs (FAs). In DSM (WSM), four (two) bands cross each other near the Fermi level (E_F). Such band crossing introduce massless Fermion nature in the low energy excitation which brings several spectacular physical properties, such as, close and open FAs,⁵ spin Hall effect (SHE),⁶ chiral anomaly^{7,8} etc. If two bands of a given crystalline material having inversion symmetries (IS) and time-reversal symmetries (TRS) cross each other in the momentum space, it can host a Dirac like quasi particle excitation near the nodal point. Such quasi particle excitation can be well captured by the relativistic Dirac equation, hence the name DSM. Whether the DSM phase is stable or fragile, it depends on crystal symmetry. For instance, under the TRS preserving condition, the Dirac nodes are stable in systems with a particular space group symmetry. The four-fold Dirac node splits into two two-fold Weyl nodes with opposite chiralities if either of the IS or TRS is broken.

So far, DSM or WSM compounds with point like Fermi surface (FS) (Fig. 1(a)) at the nodal points have been studied extensively and referred as type-I semimetals.^{9–12} There are classes where these Dirac or Weyl nodes get sufficiently tilted in the momentum space shifting the point like FS to a contour like FS (Fig. 1(b)). Such contour like FS yields strikingly different physics as compared to type-I semimetal, and are called type-II DSM or

WSM. Details of a general model Hamiltonian describing the band topology for type-II DSM and WSM are given in Sec. I of the supplemental material (SM).¹³

Till date, several type-I DSM compounds have been theoretically predicted and experimentally verified through the photo-emission and transport measurements. In contrast, only a handful number of type-II DSM^{16,17,19,20} compounds are investigated. The major problem of the existing compounds are the position of nodal points which are far from the E_F and the presence of additional trivial Fermi pockets. For example, extensively studied compounds PtSe_2 ¹⁹ and PtTe_2 ^{17,21} have type-II Dirac node around 1 eV below E_F with several trivial band crossings. VAl_3 ²² is another type-II DSM class where nodal points lie above E_F and restrict the photo-emission experiments to probe them. In this paper, using *first principle calculations*, (see Sec. II of SM¹³ for computational details) we predict three full Heusler alloys XInPd_2 ($\text{X}=\text{Ti, Zr, Hf}$) to showcase the type II DSM properties. This study can guide not only the future photoemission experiments to probe the SSs, but also shed light on the currently debated topic of fragile nature of Fermi arcs and their associated topological origin. Although there exists another compound in this class YPd_2Sn ,²³ but a detailed study of topological Fermi arcs, SSs and bulk FS driven Lifshitz transition (LT) is lacking. One of the important features of ZrInPd_2 and HfInPd_2 is that they show superconducting phase transition at temperature 2.19 K and 2.86 K respectively.^{26,27} Previously, topological superconductivity (TSC) have been studied in a general framework of Fermi loop (FL) topology and C_n rotational symmetry lowering in DSM.^{24,25} For example, Dirac compound Cd_3As_2 shows superconductivity under pressure.²⁸ With the unique orbit-momentum locking near the nodes and the C_4 to C_2 rotational symmetry lowering creates a gap at the nodal points which is speculated to stabilize the

TSC phase by increasing the condensation energy.²⁴ In contrast to the type-I DSM, bulk FS of type-II DSM is composed of non-trivial electron and hole pockets which may contribute to the formation of the Cooper pairs and allow the compound to become superconducting.³¹ Although, very recently, PdTe₂²¹ and YIn₃²⁹ type-II DSM class have been put forward to ignite the TSC study but these two classes face certain limitations similar to those of PtTe₂ and PtSe₂, as discussed above. Our full Heusler compound ZrInPd₂ is much more superior in the above contexts as its type-II Dirac node lie almost at E_F with relatively less number of Fermi pockets.

Results and Discussions: The full Heusler compounds XInPd₂ belong to the space group $Fm\bar{3}m$ ³⁰ where X and In have the equivalent Wyckoff positions (0,0,0) and (1/2,1/2,1/2) to form a rock-salt structure and Pd takes sits at (1/4,1/4,1/4) and (3/4,3/4,3/4). The primitive unit cell is shown in Fig. 1(c). The bulk Brillouin zone (BZ) and projected (001) and (111) surface BZ are shown in Fig. 1(d).

The general formation mechanism of Dirac Fermion states have been discussed in Sec. III of SM¹³ considering the point group symmetry of XInPd₂. We took ZrInPd₂ as a test case and discussed the detail calculated results. Figure 1(e) shows the band structure of ZrInPd₂ without spin orbit coupling (SOC). At the Γ point near E_F , the major contribution comes from the Zr- t_{2g} orbitals and band above this has dominant Zr- e_g contribution. Zr- t_{2g} split into E and B₂ bands along Γ -X direction whereas e_g transform into two singly degenerate A₁ and B₁ bands, denoted according to the IRs of C_{4v} little group. A₁ and B₂ bands cross each other to form a 2-fold nodal point and A₁ intersect with E to form a 3-fold nodal point as shown in Fig. 1(e). Inclusion of SOC doubles the eigen space according to double group representation of C_{4v} . Therefore, e_g transform as: $e_g \rightarrow \Gamma_8^+$ and $e_u \rightarrow \Gamma_8^-$. However, t_{2g} splits into Γ_8^+ and Γ_7^+ (i.e, $t_{2g} \rightarrow \Gamma_8^+ \oplus \Gamma_7^+$) at Γ point. In contrast, along Γ -X direction, A₁ and B₂ transform into Γ_6 and Γ_7 respectively, whereas E transform as: $E \rightarrow \Gamma_6 \oplus \Gamma_7$ as shown in Fig. 1(e,f). Note that the 2-fold Γ_7^+ IR in Fig. 2(f) propagate as Γ_7 and simultaneously 4-fold Γ_8^+ goes into Γ_6 and Γ_7 along Γ -X direction. The dimensional degeneracy of Γ_6 and Γ_7 IRs are two. Hence, accidental band degeneracy of these Γ_6 and Γ_7 bands form three Dirac nodes along Γ -X as denoted by DP1, DP2 and DP3 in Fig. 1(f). Figure 1(g) shows the zoomed view of DP1, DP2 and DP3. For DP1 and DP3, the electron (green) and hole (red) bands, which have similar slope, cross each other to form type-II Dirac nodes. However, DP2 is the type-I like Dirac node owing to the opposite electron and hole band slope. The type-II Dirac node (DP1) lies almost at E_F with small Fermi pockets away from the nodal point. The nature of all these nodal points have been explained using the effective $k.p$ Hamiltonian, as discussed Sec. IV of SM.¹³ The Chern number (topological index) for a Dirac node is zero as the nodal point can be considered as superposition of two Weyl nodes with opposite topological charges

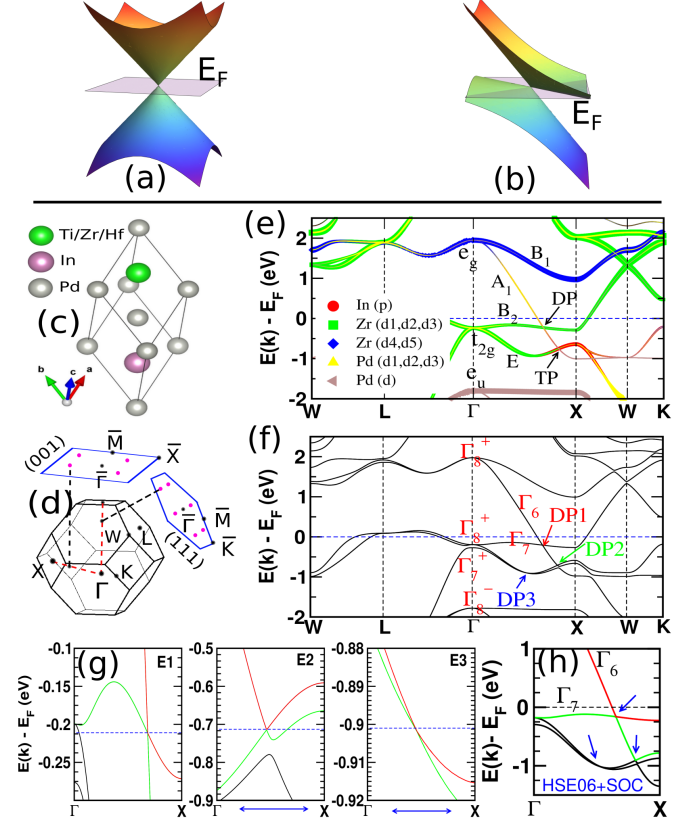


FIG. 1. (Color online) (a) Type-I Dirac node and corresponding point like Fermi surface (FS) at the nodal point. (b) Type-II Dirac node and corresponding contour like FS. (c) Crystal structure of XInPd₂. (d) Bulk and surface Brillouin zones. For ZrInPd₂, (e) orbital projected bulk band structure without SOC. (f) Bulk band structure with SOC. (g) Zoomed view of (f) near the three nodal points DP1, DP2, and DP3 at energy E1, E2 & E3 respectively. (h) HSE06+SOC band structure along Γ -X direction.

± 1 . Vanishing of Chern number for a Dirac node and its consequences on the Dirac Fermi arcs will be discussed extensively in the subsequent sections. Unlike Na₃Bi¹⁴ or Cd₃As₂,¹⁵ where non-trivial band inversion ($Z_2=1$) harbors Dirac crossings, our predicted XInPd₂ do not show band inversion and hence the Dirac nodes are manifested by accidental trivial band crossings. Further, to make sure about the topology and location of these Dirac nodes, a more accurate HSE06 level calculations are also carried out. This calculations give similar results as that of PBE calculation with Dirac nodes more closer to Fermi level, as shown in Fig. 1(h).

To reconfirm the formation of DSM phase in ZrInPd₂, we shall now illustrate the above discussion based on the structural and chemical environmental dependent crystal field theory. In full-Heusler alloy, e.g., ZrInPd₂, In atom sits at the center of an octahedra formed by Zr atoms (which sit at the six faces of FCC lattice) as shown in Fig. 2(a). Furthermore, Zr and In atoms form two inter-penetrating tetrahedra (mutually rotated by 90°)

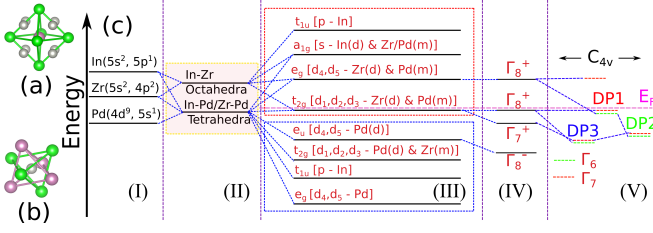


FIG. 2. (Color online) (a) Zr-In Octahedra (b) Two interpenetrating tetrahedral configuration in ZrInPd_2 . (c) Effect of orbital hybridization, crystal field splitting and formation of Dirac nodes. Region (I) is the atomic energy levels according to Aufbau principle, region (II) represents the energy level formation of octahedra and tetrahedra. Region (III) & (IV) describe the effect of crystal field splitting at Γ point without and with SOC respectively. The bands are designated with their irreducible representations (IRs). Region (V) shows the band representations and formation of nodal points along Γ -X direction or C_{4v} axes. ‘d’ and ‘m’ represent Major and minor contributions respectively from a particular atom.

keeping Pd atom at the center of tetrahedra as shown in Fig. 2(b). The atomic energy level distributions and the effect of crystal field splitting are shown in Fig. 2(c). The shaded box in region II is the pictorial representation of energy levels of octahedra and tetrahedra in the lattice. Region III represents the effect of orbital hybridization and crystal field splitting in the absence of SOC at the Γ point. In region III, the red block (above E_F) corresponds to the energy levels, mainly contributed by octahedral symmetry and the blue block (below E_F) contain the energy levels corresponding to tetrahedral symmetry. The crystal field splitting of d -orbital, due to the O_h environment (in the red block), is further emphasized. The t_{2g} orbitals which are mainly contributed by Zr, lie just below E_F whereas the e_g orbital lie above E_F . Here, in region III, d_1 , d_2 , d_3 , d_4 and d_5 represent the d_{xy} , d_{yz} , d_{xz} , $d_{x^2-y^2}$, and d_{z^2} orbitals respectively. Above the e_g level, a_{1g} and t_{1u} are mainly contributed by In s and p like orbital respectively. This is consistent with the point group formalism because the basis function for a_{1g} is spherically symmetric whereas it is linear for t_{1u} . On the other hand, the lower blue block shows the d orbital splitting in tetrahedral environment. Due to the tetrahedral splitting, the e_g orbital falls below the t_{2g} orbital. Note that, though the tetrahedra does not possess IS but the presence of global IS of the crystal structure enforces the definite parity states to the energy levels of tetrahedra. Region IV shows band splitting due to SOC. Inclusion of SOC, transform the t_{2g} octahedra level as: $t_{2g} \rightarrow \Gamma_8^+ \oplus \Gamma_7^+$. On the other hand e_g goes to Γ_8^+ . Furthermore, the e_u level transform as Γ_8^- . Region V represents the transformation of bands along Γ -X direction starting from Γ point. The detail mechanisms on formation of three Dirac nodes (DP1, DP2 and DP3) have been discussed in previous paragraph.

We will now proceed to understand the bulk FS topology, Lifshitz transition and Lorentz symmetry breaking,

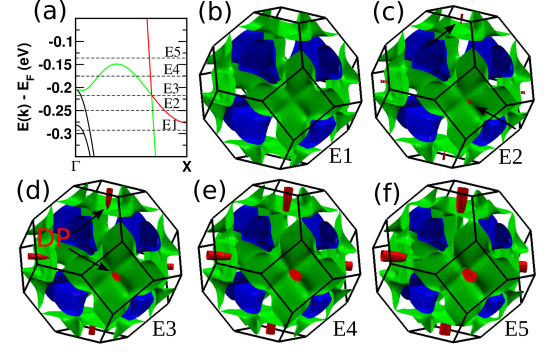


FIG. 3. (Color online) (a) Zoomed band structure of ZrInPd_2 along Γ -X direction. E1-E5 are different energy cuts around the type-II Dirac node DP1. (b-f) Bulk Fermi surface at different energy cuts E1-E5.

for which bulk FS near nodal point DP1 is simulated. The simplest Hamiltonian describing a type-II Weyl node is, $H = c\vec{\sigma} \cdot \vec{p} + vp_z$.^{31,32} The second term in H tilt the cone along z -direction in the momentum space depending on the relative magnitude of v . For $v = 0$, the cone is not tilted, it become a type-I semimetal which have point like FS at the nodal point (Fig. 1(a)). For $0 < v < c$, the cone is tilted. If $v > c$, the cone is over tilted which results the Fermi level to cross the electron and hole bands, forming contour like Fermi surface connected by the Weyl point, called type-II semimetal (Fig. 1(b)). The Lifshitz transition occurs for $v = c$ between these two types of cone. The above scenario is similarly applicable for Dirac nodes but need extra crystalline symmetry to stabilize the Dirac point. Figure 3(a) shows a zoomed view of bulk band structure along Γ -X with five energy cuts E1-E5. Figure 3(b-f) shows the bulk Fermi surface for respective energy cuts. The red(green) bands indicate the electron(hole) type. For E1 energy cut, the electron type FSs are completely absent where as for E2, a tiny electron FS appear as shown by the arrowhead. E3 corresponds to the nodal point energy and the type-II Dirac nodes are indicated by arrowhead in Fig. 3(d). The electron band contribution in the FSs for E4 and E5 energy cut increases progressively. Further, FS maps have been projected on a 2D plane to get clear view on the evolution of electron and hole pockets near the DP as shown in Fig. S2.¹³ The FSs evolution justify the tilting of Dirac nodes in the momentum space and breaking of Lorentz symmetry. Here, the crystalline symmetry allows such tilting of cones in low energy system without respecting the Lorentz invariance. Although, DP1 in Fig. 1(f,h) indicates a type-II Dirac cone, the band effective mass of Γ_6 and Γ_7 clearly hints that the cone is in near critical region (i.e., $v = c$) between type-I and type-II Dirac states. Similar observations of Fermi surface topology have previously been seen in type-II Dirac and Weyl semimetals and commonly referred as Lifshitz transition in Ref. [23,33]. Such transition is unique by itself (responsible for exotic phenomenon), and is attributed to the occurrence

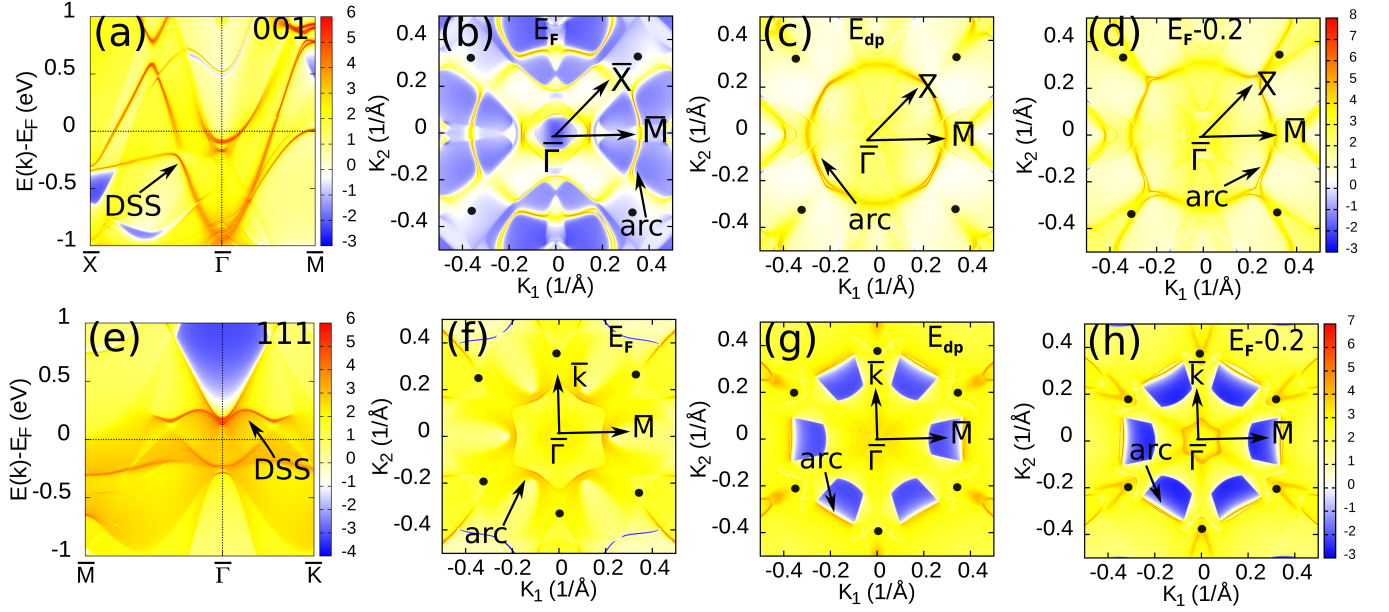


FIG. 4. (Color online) Surface states (SSs) and Fermi arcs (FAs) of ZrInPd_2 using Green's function method. (a) SSs of (001) surface and (b-d) corresponding FAs for different energy cuts. (e) SSs of (111) surface and (f-h) corresponding FAs for different energy cuts.

of superconductivity in ZrInPd_2 .

Similar to the WSM, DSMs also hold the signature of bulk band degeneracies onto its surfaces. Since one Dirac node can be viewed as superposition of two Weyl nodes, double Fermi arcs (FAs) are expected on the bulk projected surfaces. The topological character of such DSM phase can further be understood from the fragility nature of the surface FAs. Hence surface dispersion and FAs of DSM are worthy of careful investigation both from theoretical and experimental front. To reveal the topological nature of FAs, we investigated the (001) and (111) surfaces. There are six Dirac nodes situated along the six Γ -X direction in the first BZ, as shown in the Fig. 1(d). Of these six, four are projected on the (001) surface (indicated by pink dot along $\bar{\Gamma} - \bar{X}$ direction on (001) surface) and the other two on the $\bar{\Gamma}$ point. If we consider that these projected nodes are the source and sink of the surface arcs (though it is not absolutely true for DSM nodes, that will be discussed in detail in the next paragraph), it is expected to get a square like close Fermi loop on (001) surface. However, the (111) surface contains six projected Dirac points as indicated by pink dot along $\bar{\Gamma} - \bar{K}$ direction on (111) surface BZ. Hence, a hexagonal shaped FA expected on this surface. Figure 4(a) shows the (001) SS of ZrInPd_2 for Zr-In terminated surface. FAs of (001) surface for different energy cuts are shown in Fig. 4(b-d). Fig. 4(e) shows the (111) SS for Zr terminated surface and Fig. 4(f-h) the corresponding FAs at different energy cuts. In Fig. 4(b-d & f-h), arcs are simulated using green's function method at E_F , energy of DP1 (E_{dp}) and 0.2 eV below E_F ($E_F - 0.2$) to show their

evolution on both (001) and (111) surfaces. The evolution clearly shows the fragile nature of Dirac arcs and further hints about their topological features. We have also calculated the SSs of both (001) and (111) surface using slab method within the *ab-initio* framework (see Fig. S1 (a,b) in SM¹³). Details about the slab model calculation is discussed in Section V of SM.¹³

M. Kargarian *et al.*³⁴ and Yun Wu *et al.*³⁵ have proposed the fragile nature of Dirac arcs which deform into a Fermi contour, strikingly different from the concept of Chern number protected Weyl arcs and similar to the surface states of a topological insulator. Such Fermi contour may convert to a loop and can also merge into the bulk projected surface Dirac nodes upon the variation of chemical potentials on the surface.³⁵ The fragile nature of Dirac FAs supports the zero Chern number of Dirac nodes and the absence of topological index mediated protections (although it can be stabilized by certain crystalline symmetry). Figure 4(b) is the Fermi arc exactly at the E_F on (001) surface. It is clear from the figure that the arcs are completely disconnected from the bulk projected surface Dirac nodes and they do not even form a close loop. This is different from the nature of Weyl arcs and indeed justify the absence of topological robustness in the bulk system. Interestingly, upon varying the chemical potentials, arcs deformed into the Fermi loop which is again not connected with the projected Dirac nodes, as observed in Fig. 4(c). The Fermi loop, however, sink into surface DPs with further lowering of chemical potential, as shown in Fig. 4(d). For (111) surface, the topological nature of arcs, as shown in Fig. 4(f-h), are

similar to that of (001) surface. The arc form a loop shape in Fig. 4(f). However, they are connected with bulk states in Fig. 4(g,h) at other energy windows. Such detailed analysis not only guide the experimentalists to correctly probe the SSs but also establish a strong base to the largely debated topic of the topological nature of Dirac arcs. The take home message of the entire discussion is that a little perturbation in the bulk crystal that do not disturb the responsible crystalline symmetry for the Dirac state can deform the surface FAs to a disconnected Fermi contour. However, these arcs may not be completely destroyed because of the presence of crystal mirror invariant planes which can further provide mirror Chern number protection.

In addition to ZrInPd_2 , we have simulated the band structure of TiInPd_2 and HfInPd_2 as well and found quite interesting type-II Dirac semi-metal features. The type-II Dirac nodes lie very close to E_F for both the compounds, as shown in Fig. S3(a,b) in SM.¹³ The SSs and Fermi arcs are expected to be similar to ZrInPd_2 , as they possess very similar bulk band topology. We have discussed the energy location of the DPs for XInPd_2 and compared with previously studied type-II DSMs in Sec. VII of SM.¹³

Conclusion: In summary, we have predicted three full Heusler compounds XInPd_2 ($X = \text{Ti, Zr and Hf}$) as potential candidates for type-II DSM. Among them, ZrInPd_2 and HfInPd_2 has been experimentally synthesized and measured to undergo superconducting transition at 2.19K and 2.86K. The position of the nodal points lie at/near E_F which should facilitate for strong response in the transport measurements. Unlike extensively studied PtTe_2 class of compounds, our predicted compounds are more superior for experimental investigation because

of the location of nodal point in close vicinity of E_F and relatively less number of trivial Fermi pockets. In the present systems, another type-I and type-II Dirac nodes coexist at a little lower energy along Γ -X. We have carefully studied the bulk FSs at different energy cuts near type-II node (DP1) to investigate the breaking of Lorentz symmetry, tilting of cone and possible Lifshitz transition (LT) of FS. The bulk FSs indicate that ZrInPd_2 lie near the boundary of type-I and type-II semimetal (i.e., at the LT region) which could be an underlying reason for the superconducting transition in these systems. SSs and Fermi arcs are simulated on (001) and (111) surfaces of ZrInPd_2 to investigate the bulk boundary correspondence and their topological nature. Our detail analysis of Fermi arcs not only guide the experimentalists to reliably probe the SSs but also shed light on the largely debated topic of the topological nature of Dirac arcs. We conclude that a little perturbation in the bulk crystal, that do not disturb the responsible crystalline symmetry for the Dirac state, can deform the surface Fermi arcs to a disconnected Fermi contour. As such, the Dirac Fermi arcs are fragile in nature and does not have topological protection like Weyl arcs. SSs are also simulated using slab model. Thus, we believe that XInPd_2 possibly stands as the most ideal material, yet proposed, to host type-II DSM state. We strongly encourage experimental investigations to reconfirm our findings.

This work is financially supported by DST SERB (EMR/2015/002057), India. We thank IIT Indore and IIT Bombay for the lab and computing facilities. CKB and CM acknowledge MHRD-India for financial support. AA acknowledges IRCC early career research award project, IIT Bombay (RI/0217-10001338-001) to support this research.

* These two authors have contributed equally to this work

† biswarup@iiti.ac.in

‡ aftab@iitb.ac.in

¹ S. M. Young, S. Zaheer, J. C. Y. Teo, C. L. Kane, E. J. Mele, and A. M. Rappe, *Phys. Rev. Lett.* **108**, 140405 (2012).

² Benjamin J. Wieder, Youngkuk Kim, A.M. Rappe, and C.L. Kane, *Phys. Rev. Lett.* **116**, 186402 (2016)

³ N.P. Armitage, E.J. Mele, and Ashvin Vishwanath, *Rev. Mod. Phys.* **90**, 015001 (2018).

⁴ Su-Yang Xu, Ilya Belopolski, Nasser Alidoust, Madhab Neupane, Guang Bian *et al.* *Science* **349**(6248), 613 (2015).

⁵ Sahin K. Özdemir, *Science* **359** (6379), 995 (2018).

⁶ Joseph Maciejko, Taylor L. Hughes, and Shou-Cheng Zhang, *Annu. Rev. Condens. Matter Phys.* **2**, 31 (2011).

⁷ Jan Behrends, Adolfo G. Grushin, Teemu Ojanen, and Jens H. Bardarson, *Phys. Rev. B* **93**, 075114 (2016).

⁸ Sihang Liang, Jingjing Lin, Satya Kushwaha, Jie Xing, Ni Ni, R.J. Cava, and N.P. Ong, *Phys. Rev. X* **8**, 031002 (2018).

⁹ Gang Li, Binghai Yan, Zhijun Wang, and Karsten Held,

Phys. Rev. B **95**, 035102, (2017)

¹⁰ Z. K. Liu, J. Jiang, B. Zhou, Z. J. Wang *et al.* *Nature Materials* **13**, 677681, (2014)

¹¹ Z. K. Liu, B. Zhou, Y. Zhang, Z. J. Wang *et al.* *Science* **343**, 864867, (2014)

¹² Wendong Cao, Peizhe Tang, Yong Xu, Jian Wu, Bing-Lin Gu, and Wenhui Duan, *Phys. Rev. B* **96**, 115203, (2017)

¹³ See Supplemental Material at [URL] for details about computational methodology, symmetry analysis, model Hamiltonian, surface calculation using slab model, 2D Fermi surface maps.

¹⁴ Zhijun Wang, Yan Sun, Xing-Qiu Chen, Cesare Franchini, Gang Xu, Hongming Weng, Xi Dai, and Zhong Fang, *Phys. Rev. B* **85**, 195320 (2012).

¹⁵ Zhijun Wang, Hongming Weng, Quansheng Wu, Xi Dai, and Zhong Fang, *Phys. Rev. B* **88**, 125427 (2013).

¹⁶ Tay-Rong Chang, Su-Yang Xu, Daniel S. Sanchez, Wei-Feng Tsai *et al.* *Phys. Rev. Lett.* **119**, 026404 (2017).

¹⁷ Mingzhe Yan, Huaqing Huang, Kenan Zhang, Eryin Wang, Wei Yao, *et al.* *Nat. Commun.* **8**, 257 (2017).

¹⁸ Han-Jin Noh, Jinwon Jeong, En-Jin Cho, Kyoo Kim, B.I. Min, and Byeong-Gyu Park, *Phys. Rev. Lett.* **119**, 016401

- (2017).
- ¹⁹ Huaqing Huang, Shuyun Zhou, and Wenhui Duan, Phys. Rev. B **94**, 121117(R) (2016).
 - ²⁰ Amit, R. K. Singh, Neha Wadehra, S. Chakraverty, and Yogesh Singh, Phys. Rev. Materials **2**, 114202 (2018).
 - ²¹ R. C. Xiao, P. L. Gong, Q. S. Wu, W. J. Lu, M. J. Wei, J. Y. Li, H. Y. Lv, X. Luo, P. Tong, X. B. Zhu, and Y. P. Sun, Phys. Rev. B **96**, 075101 (2017).
 - ²² K.-W. Chen, X. Lian, Y. Lai, N. Aryal, Y.-C. Chiu, W. Lan, D. Graf, E. Manousakis, R.E. Baumbach, and L. Balicas, Phys. Rev. Lett. **120**, 206401 (2018).
 - ²³ Peng-Jie Guo, Huan-Cheng Yang, Kai Liu, and Zhong-Yi Lu, Phys. Rev. B **95**, 155112 (2017).
 - ²⁴ Shingo Kobayashi and Masatoshi Sato, Phys. Rev. Lett. **115**, 187001, (2015)
 - ²⁵ Shengyuan A. Yang, Hui Pan, and Fan Zhang, Phys. Rev. Lett. **113**, 046401, (2014)
 - ²⁶ Jürgen Winterlik, Gerhard H. Fecher, Anja Thomas, and Claudia Felser, Phys. Rev. B **79**, 064508 (2009).
 - ²⁷ T. Klimczuk, C. H. Wang, K. Gofryk, F. Ronning, J. Winterlik, G. H. Fecher, J.-C. Griveau, E. Colineau, C. Felser, J. D. Thompson, D. J. Safarik, and R. J. Cava, Phys. Rev. B **85**, 174505 (2012).
 - ²⁸ Lanpo He, Yating Jia, Sijia Zhang, Xiaochen Hong, Changqing Jin & Shiyang Li, npj Quantum Materials **1**, 16014 (2016).
 - ²⁹ Xin-Hai Tu, Peng-Fei Liu, and Bao-Tian Wang, Phys. Rev. Materials **3**, 054202 (2019).
 - ³⁰ Heusler Alloys Properties, Growth, Applications, Claudia Felser & Atsufumi Hirohata, Springer.
 - ³¹ Dingping Li, Baruch Rosenstein, B. Ya. Shapiro, and I. Shapiro, Phys. Rev. B **95**, 094513 (2017).
 - ³² G E Volovik, Phys.-Usp. **61**, 89 (2018) and references therein.
 - ³³ Alexey A. Soluyanov, Dominik Gresch, Zhijun Wang, QuanSheng Wu, Matthias Troyer, Xi Dai & B. Andrei Bernevig, Nature **527**, 495 (2015).
 - ³⁴ Mehdi Kargarian, Mohit Randeria, and Yuan-Ming Lu, PNAS **113** (31), 8648 (2016).
 - ³⁵ Yun Wu, Na Hyun Jo, Lin-Lin Wang, Connor A. Schmidt, Kathryn M. Neilson *et al.* Phys. Rev. B **99**, 161113(R) (2019).